Ringing Loads on Tension Leg Platform Wind Turbines

Erin E. Bachynski[a,b,*], Torgeir Moan[a,b]

[a] *Centre for Ships and Ocean Structures, NTNU, NO-7491 Trondheim, Norway*
[b] *Centre for Autonomous Marine Operations and Systems, NTNU, NO-7491 Trondheim, Norway*

Abstract

The present work identifies realistic wave (and associated wind) conditions which could induce ringing responses in tension leg platform wind turbines (TLPWTs). The simulation results show the importance of ringing forces, the effects of turbine operation, and the sensitivity of the ringing response to platform stiffness and viscous damping.

To model the ringing loads, the second order quadratic transfer function and a bandwidth-limited summation formulation for the third order wave forces were implemented. The chosen formulation avoids the spectrum cut-off dependency and the low-frequency components of a direct implementation of the irregular wave Faltinsen, Newman, Vinje (FNV) formula. Depending on the natural period and damping, the difference between a direct implementation and this formulation was 5-25 %.

Ringing-type responses were simulated for 50-year wind and wave conditions. Various hydrodynamic models were used to isolate physics in different approaches. For platforms with 14-18 m diameters, ringing loads resulted in larger extreme loads and increased short-term fatigue damage in the tendons and tower. Ringing effects were particularly severe for platforms with a pitch/bending natural period of 3-4 seconds. The viscous damping coefficient had negligible influence on the ringing response, while aerodynamic damping could be important in damping the oscillations following the initial maximum.

Keywords: tension leg platform, offshore wind turbine, ringing

Nomenclature

a Radius

C_D Drag coefficient

D Diameter

$d\omega$ Frequency bandwidth

D_{RFC} Fatigue damage

F_t Tendon pretension

$F_x^{FNV(3)}$ Third order long-wave horizontal force

*Corresponding author, tlf: +47 73 59 52 05, fax: +47 73 59 55 28
Email address: erin.bachynski@ntnu.no (Erin E. Bachynski)

Fr Froude number

FNV Faltinsen, Newman, Vinje force formulation

g Acceleration due to gravity

h Draft (of cylinder for force calculation)

H_s Significant wave height

K Material parameter (SN curves)

k Wave number ($k = 2\pi/\lambda$)

KC Keulegan-Carpenter number

K_I Integral control coefficient

K_P Proportional control coefficient

m SN curve slope

M_{FA} Fore-aft tower base bending moment

S Stress range

T_1 Downwind tendon tension

T_p Peak period

TLP Tension leg platform

TLPWT Tension leg platform wind turbine

u Wave particle horizontal velocity

U_w Mean wind speed

w Wave particle vertical velocity

β Function representing finite cylinder depth

$\Phi^{(i)}$ Velocity potential (i-th order)

ζ Wave amplitude

λ Wavelength

ρ Water density

Ψ_1 and Ψ_2 Non-dimensional spatially varying functions

ω Wave frequency

ω_p Peak wave frequency

$\omega_{\psi n}$ Controller natural frequency

1. Introduction

Tension leg platform wind turbines (TLPWTs) hold promise for capturing offshore wind energy in intermediate (45-150 m) and deep (>150 m) water. TLPWT designs with diameters in the range 5-18 m and pitch natural periods of 1.5-4.5 seconds have been presented in the literature (Matha, 2009; Henderson et al., 2010; Bachynski and Moan, 2012; Stewart et al., 2012). Marine structures with structural periods in the range of 1-5 seconds are known to be susceptible to "ringing" responses in severe seas: "transient structural deflections at frequencies substantially higher than the incident wave frequencies" (Faltinsen et al., 1995). In contrast to the more steady-state "springing" response to sum-frequency wave effects, ringing is characterized as a transient event, generally following a high, steep wave (Gurley and Kareem, 1998). The present work seeks to identify environmental conditions that could induce ringing responses in TLPWTs and evaluate their effects.

Ringing of offshore oil and gas tension leg platforms (TLPs) is known to occur in steep wave conditions (Faltinsen et al., 1995). Ringing responses were first observed on the Hutton platform, and were subsequently seen in Heidrun and Snorre model tests (Natvig, 1994). Studies of the hydrodynamic loading which drives these responses provided significant theoretical development in the 1990's. Some of the hydrodynamic criteria for ringing loads that have been described in previous studies (Faltinsen et al., 1995; Tromans et al., 2006) include:

1. Presence of surface-piercing columns.

2. Low Keulegan-Carpenter number ($KC = 2\pi U/\omega D$, where U is the fluid particle velocity amplitude, ω is the wave period, and D is the diameter) (fluid loading dominated by inertial loads): $KC < 5$.

3. Low diameter-wavelength (D/λ) ratio (linear diffraction is not significant): $D/\lambda < 0.2$. (Alternatively: $ka < 0.63$, where $k = 2\pi/\lambda$ and $a = D/2$)

4. Wave height comparable to cross-sectional structure dimensions.

TLPWT platforms, particularly single column designs with relatively large diameters, may meet the given criteria for certain wave conditions. In order to model these forces, a model of the nonlinear forces (third order and higher) on cylindrical columns is required.

The well-known Faltinsen, Newman, Vinje (FNV) long-wave formulation (Faltinsen et al., 1995) for the horizontal forces on a vertical cylinder due to the third order potential was extended to irregular waves by Newman (1996b). While the second order component of the long-wave excitation force has been shown to compare well to full second-order diffraction only up to approximately $ka = 0.1$, the third order FNV formulation is known to compare well to full third order diffraction theory up to $ka = 0.4$ (Krokstad et al., 1998).

The approach used by Krokstad et al. (1998) was therefore followed here: the full second order sum-frequency quadratic transfer function (QTF) forces were included in all degrees of freedom, and the third order sum-frequency horizontal forces according to the FNV formulation were added. The explicit expression for the pitch moment based on Marthinsen et al. (1996) was not included in the present formulation. The expression for the ringing moment is not fully consistent, and is expected to be less important than the moment about the center of gravity induced by the horizontal force applied at the still water level.

Even using the second order QTF rather than the second order FNV component, Krokstad et al. (1998) found that the FNV formulation slightly overpredicted the high-frequency loads on

a stationary cylinder. The overprediction was steepness-dependent, with steeper waves leading to larger overprediction. Stansberg (1997) presented experimental results for the first, second, and third order loads on fixed cylinders of different diameters. Although similar overprediction of the forces was observed, the FNV model was shown to correctly predict the trends in the third order force with regards to wave number.

An alternative implementation of the FNV formulation for irregular waves was presented by Johannessen (2012). This implementation addresses two of the challenges associated with a direct implementation of FNV: the spectrum cut-off dependency and the presence of low-frequency components. FNV includes terms that do not decay at high frequency, which implies that nonphysical wave components can be amplified, and the resulting force can be altered based on the input wave spectrum. Additionally, a direct implementation of the irregular FNV formula includes undesired difference-frequency components (Newman, 1996a).

In the present work, two methods of computing the ringing force were considered: a direct implementation of Newman's irregular wave formulation (Newman, 1996b), and Johannessen's bandwidth-limited, sum-frequency-only implementation (Johannessen, 2012). After comparing the computed forces and examining the response of a single degree-of-freedom model, Johannessen's formulation was chosen for use in the time-domain coupled simulations of several TLPWT models, as it removes some of the overconservatism of the direct implementation while preserving the desired terms.

Neither of the aforementioned approaches can capture the secondary loading cycle that was experimentally observed as early as 1993 by Grue et al. (1993). This loading cycle, which was documented for moderately steep waves and relatively large radii ($k\zeta > 0.3$, $0.1 < ka < 0.33$, $3.8 < KC < 7$ and $Fr > 0.4$, where $Fr = \omega A/\sqrt{gD}$), takes place approximately one quarter wave period after the main force peak (Grue and Huseby, 2002). This phenomenon may also affect TLPWTs with very large diameters, but cannot be modeled by current numerical methods and is not considered here.

Although ringing forces on TLPWTs have not been studied until now, nonlinear shallow water wave effects on bottom-fixed monopile offshore wind turbines have been investigated. Rogers (1998) examined breaking wave effects on monopiles and observed ringing-type responses. Significant harmonic structures up to the 5th order in the wave forces on a monopile during focused wave experiments have been observed, even in the absence of breaking waves (Zang et al., 2010). Furthermore, several authors have investigated the effects of nonlinear models. Veldkamp and van der Tempel (2005) observed 5-10 % differences in the predicted fatigue damage on monopiles due to the use of second order or fully nonlinear waves, and more recent irregular wave simulations of a monopile wind turbine indicated that severe sea states contribute more significantly to the fatigue damage using nonlinear wave forcing compared to linear wave forcing (Schløer et al., 2013).

In the present work, the hydrodynamic developments from TLPs are applied to TLPWTs and the responses, including the wind turbine, are considered. The different ringing force formulations are introduced in Sec. 2. The computational tool, environmental conditions, TLPWT models – including a modification to the control system – and fatigue damage estimation method are presented in Sec. 3, while results for the baseline designs, softened designs, and variations in turbine operational status and viscous damping are shown in Sec. 4.

2. Third order ringing force formulations

Two methods of computing the ringing force are described in Sections 2.1 and 2.2: a direct implementation of Newman's irregular wave formulation (Newman, 1996b), and Johannessen's

bandwidth-limited, sum-frequency-only implementation (Johannessen, 2012). Simulations of a simple mass-spring-dashpot system subjected to normalized wave forces according to the different formulations are presented in Section 2.3.

2.1. Direct computation of irregular wave FNV

For an infinitely deep, surface-piercing vertical circular cylinder, the third order force due to the first order potential is given by Newman (1996b):

$$F_3^{(1)} = \pi\rho a^2 \left[\zeta_1 \left(u_{tz}\zeta_1 + 2ww_x + uu_x - \frac{2}{g}u_t w_t\right) - \left(\frac{u_t}{g}\right)\left(u^2 + w^2\right)\right] \tag{1}$$

where ρ is the water density, g is the acceleration due to gravity, ζ_1 is the first order wave elevation, and u and w are the horizontal and vertical wave particle velocity, respectively. Differentiation is indicated by subscripts. The third order force due to the nonlinear (second order) potential is given as:

$$F_3^{(2)} = \frac{\pi\rho a^2}{g} u^2 u_t \beta \tag{2}$$

where

$$\beta = \int_0^{(h+\zeta_1)/a} \left(3\Psi_1 + 4\Psi_2\right) dZ, \tag{3}$$

h is the cylinder draft, and $\beta = 4$ for an infinitely long cylinder. The definitions of the non-dimensional functions $\Psi_1(Z)$ and $\Psi_2(Z)$ (spatially-varying components of the solution to Laplace's equation for a stationary vertical cylinder) can be found in (Faltinsen et al., 1995; Newman, 1996b). Finally, the third order horizontal force may be implemented directly as in Eq. 4.

$$F_x^{FNV(3)} = F_3^{(1)} + F_3^{(2)} \tag{4}$$

A direct implementation of irregular wave FNV is straightforward to implement. Given the wave components, pre-generation of the third order force is computationally inexpensive. Generation of the third order force during the dynamic simulation (including corrections for platform position) does not increase the dynamic simulation time significantly.

2.2. Bandwidth-limited, sum-frequency implementation

Johannessen (2012) calculates the third order force as

$$F_x^{FNV(3)} = \rho\pi a^2 \left(2\zeta_2\Phi_{xt}^{(1)} + \zeta_1^2\Phi_{xtz}^{(1)} + \zeta_1\Phi_z^{(1)}\Phi_{xz}^{(1)} + \frac{\beta}{g}{\Phi_x^{(1)}}^2\Phi_{xt}^{(1)}\right) \tag{5}$$

(where the original formulation is given for $\beta = 4$), using a different perturbation for ζ_2. Rewriting Johannessen's formulation in terms of particle velocities gives:

$$F_x^{FNV(3)} = \rho\pi a^2 \left(2\zeta_2 u_t + \zeta_1^2 u_{tz} + \zeta_1 ww_x + \frac{\beta}{g}u^2 u_t\right) \tag{6}$$

which is equivalent to Eq. 4 except for difference-frequency terms, but Eq. 6 is only strictly valid for wavenumber sum terms Johannessen (2012). By writing the wave potential as a sum of N linear wave components:

$$\Phi^{(1)} = \sum_{n=1}^{N} a_n \frac{\omega_n}{k_n} \sin(\phi_n) e^{k_n z} \tag{7}$$

where $\phi_n = k_n x - w_n t + \epsilon_n$ and deep water is assumed, Johannessen (2012) writes the third order FNV force as in Eqs. 8-10. These equations, which do not include any difference-frequency terms, are reproduced here in an effort to clarify the misprinted subscripts in the original paper.

$$\begin{aligned} 2\zeta_2 \Phi^{(1)}_{xt} + \zeta_1^2 \Phi^{(1)}_{xtz} =& \frac{g}{4} \sum_{n=1}^{N} \Bigg(3a_n^3 k_n^2 \sin(3\phi_n) \\ &+ \sum_{m=1}^{n-1} \Bigg(a_n a_m (a_n (2k_n + k_m)^2 \sin(2\phi_n + \phi_m) \\ &+ a_m (k_n + 2k_m)^2 \sin(\phi_n + 2\phi_m)) \\ &+ \sum_{j=1}^{m-1} 2a_n a_m a_j ((k_n + k_m + k_j)^2 \sin(\phi_n + \phi_m + \phi_j)) \Bigg) \Bigg) \end{aligned} \tag{8}$$

$$\begin{aligned} \zeta_1 \Phi^{(1)}_z \Phi^{(1)}_{xz} =& \frac{1}{4} \sum_{n=1}^{N} \Bigg(a_n^3 \omega_n^2 k_n \sin(3\phi_n) \\ &+ \sum_{m=1}^{n-1} \Bigg(a_n a_m (a_n \omega_n (k_n \omega_n + k_m \omega_m + k_n \omega_m) \sin(2\phi_n + \phi_m) \\ &+ a_m \omega_m (k_n \omega_n + k_m \omega_m + k_m \omega_n) \sin(\phi_n + 2\phi_m)) \\ &+ \sum_{j=1}^{m-1} a_n a_m a_j (((k_n \omega_n + k_m \omega_m)\omega_j + (k_n \omega_n + k_j \omega_j)\omega_m \\ &+ (k_j \omega_j + k_m \omega_m)\omega_n) \sin(\phi_n + \phi_m + \phi_j)) \Bigg) \Bigg) \end{aligned} \tag{9}$$

$$\begin{aligned} \frac{\beta}{g} {\Phi^{(1)}_x}^2 \Phi^{(1)}_{xt} =& \frac{\beta}{2} \sum_{n=1}^{N} \Bigg(\frac{1}{2} a_n^3 \omega_n^2 k_n \sin(3\phi_n) \\ &+ \sum_{m=1}^{n-1} \Bigg(a_n a_m \big(a_n k_n \omega_m \big(\omega_n + \frac{\omega_m}{2} \big) \sin(2\phi_n + \phi_m) \\ &+ a_m k_m \omega_n \big(\omega_m + \frac{\omega_n}{2} \big) \sin(\phi_n + 2\phi_m) \big) \\ &+ \sum_{j=1}^{m-1} a_n a_m a_j ((k_n \omega_m \omega_j + k_m \omega_n \omega_j + k_j \omega_m \omega_n) \sin(\phi_n + \phi_m + \phi_j)) \Bigg) \Bigg) \end{aligned} \tag{10}$$

In practice, this formulation is computationally expensive for large values of N. To avoid this problem, a window function over $20T_p$ (with a taper over $2T_p$) is used when extracting the wave components, and a bandwidth limitation is applied in the calculation of the forces (Johannessen,

2012). This bandwidth limitation prevents interaction among waves of very different frequencies. The maximum allowable bandwidth $d\omega$ is chosen to be $1.4\omega_p$, where $\omega_p = 2\pi/T_p$, and T_p is the peak period. This is a larger bandwidth than Johannessen recommends based on his work at model scale, but gives good agreement with the bandwidth-filtered force time series computed using Eq. 4. Fig. 1 shows the ringing load calculated for different values of $d\omega$. As shown, there is little change in the force for $d\omega \geq 1.4\omega_p$.

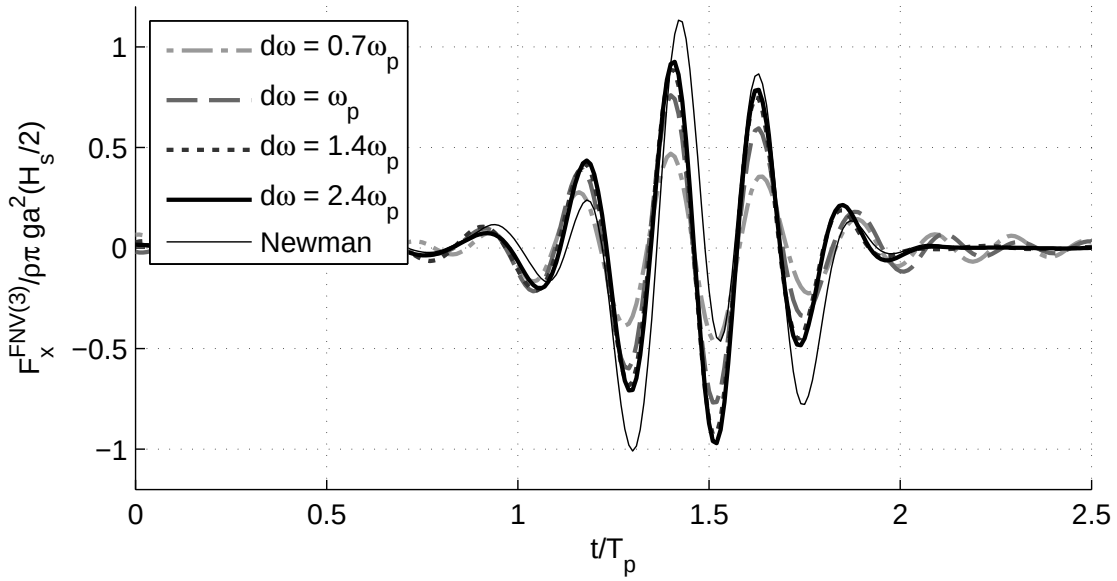

Figure 1: Ringing loads according to Eqs. 8-10 for variable bandwidth $d\omega$. $\omega_p = 0.63$ rad/s, and $H_s = 8.71$ m. The direct implementation of Newman's formula (Eq. 4) is shown for comparison.

The computational effort for this formulation depends on the length of the simulation, the bandwidth, and the size of the window for wave component extraction. It should be noted that the computational effort increases superlinearly with increasing bandwidth. For a typical 1-hour simulation, with a window function of 200 s and a bandwidth of 0.9 rad/s, Johannessen's method required approximately 40 times the computational time required for the direct implementation. The pre-generation of the loads took approximately 15 % of the time of the dynamic simulation. Improvements to the implementation can reduce the computational effort, but the triple summations are inherently more computationally intensive than the direct formulation.

2.3. Response of a 1-DOF system

The difference between the direct implementation of Newman's model and Johannessen's implementation is primarily a low-frequency component. For the waves examined here, there may be up to a 50% discrepancy in the maximum (or minimum) value of the third order force based on the two implementations, with the direct implementation of Newman's model giving larger peaks and troughs. There is a resulting 5-15% discrepancy in the maximum (or minimum) total force. In order to examine the importance of the low-frequency component on the system response, a single degree-of-freedom (DOF) model was designed to mimic the TLPWT response frequency. For a unit mass, the spring coefficient was chosen to give the desired natural period, T_n, and the linear damping coefficient was chosen to give the desired damping level.

The single DOF model's responses to normalized values of the third order force – and to normalized values of the total force, including first and second order components – were computed

and compared for 10 wave time series corresponding to large third order forces. The resulting maxima and minima are compared in Figs. 2–3.

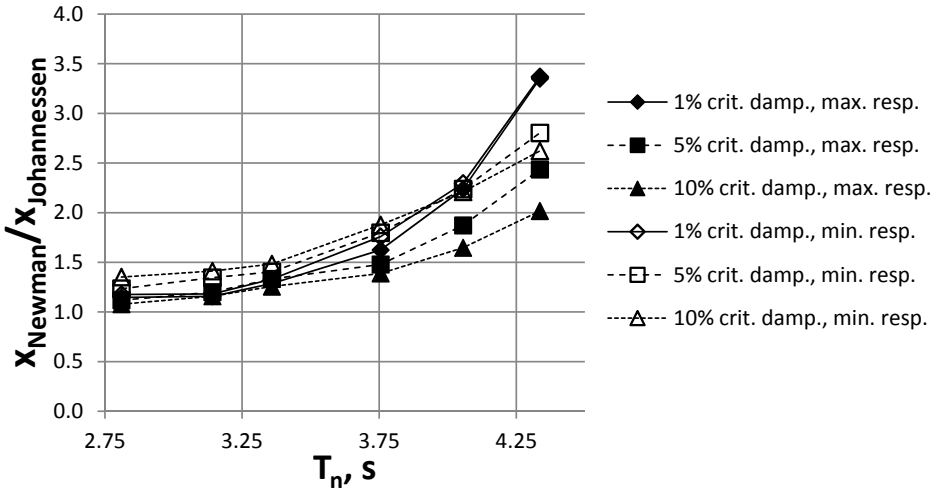

Figure 2: Average discrepancies in the single DOF system responses to the normalized third order wave force as a function of system natural period (T_n). Maximum and minimum values of the response using the direct Newman equation are divided by the corresponding values using the Johannessen force formulation.

As shown in Fig. 2, there is a large difference – up to a factor of 3 – in the response of the single DOF system to the third order force, particularly as the system natural period increases. Similar trends are noticed regardless of the damping level, but the difference in the maximum (or minimum) response tends to be largest for very lightly damped systems. The damping level has a larger impact on the responses for longer natural periods.

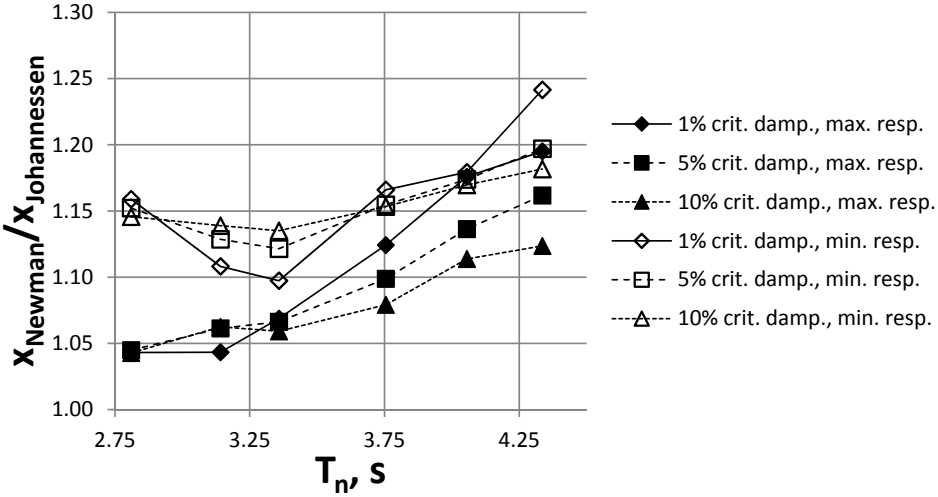

Figure 3: Average discrepancies in the single DOF system responses to the normalized total wave force as a function of system natural period (T_n). Maximum and minimum values of the response using the direct Newman equation are divided by the corresponding values using the Johannessen force formulation.

Fig. 3 shows that the impact of the different formulations on the response to the total force is, as expected, much smaller than the impact on the response to the third order force. Generally, the discrepancy increases for increasing natural period and for decreasing damping. Simulations for natural periods near those of the original TLPWT designs (around 2.81 s) show little dependence on damping, and large differences in the minimum value of the response.

Based on this investigation, the low-frequency components in a direct implementation of Newman's irregular wave FNV formula may have non-negligible effects on the extreme responses of systems with natural frequencies near those of typical TLPWT designs. Since these low-frequency components are not desired in the third order force description, Johannessen's formulation was chosen for this study. The difference between the responses was estimated to be 5-25%, depending on the natural period and damping.

3. Dynamic TLPWT simulations

Three computer codes were used to model the coupled behavior of the TLPWT systems in the time domain: SIMO, which models the rigid body hydrodynamics of the hull (MARINTEK, 2011b); RIFLEX, which includes the finite element solver, flexible elements for the tendons, tower, shaft, and blades, and the link to an external controller (MARINTEK, 2011a); and AeroDyn, which provides the forces and moments on the blades based on Blade Element/Momentum (BEM) or Generalized Dynamic Wake (GDW) theories, including dynamic stall, tower shadow, and skewed inflow correction (Moriarty and Hansen, 2005). The generator torque and blade pitch control system was written in Java. This combination provided a stable nonlinear finite element solver, sophisticated hydrodynamics, well-tested aerodynamics, and control logic. The SIMO-RIFLEX wind turbine module has been previously verified (Luxcey et al., 2011; Ormberg et al., 2011), and the SIMO-RIFLEX-AeroDyn combination is documented in Ormberg and Bachynski (2012).

In the structural model, the hull was rigid, while 10 beam elements were used for the tower, 17 beam elements were used for each blade, and the tendons were composed of approximately 60 beam elements per tendon, with cross-sectional properties computed for hollow, air-filled tubular steel sections (including bending stiffness). The anchors were modeled by nodes that were fixed in translation and free in rotation, such that the tendons were pinned to the rigid seabed. Pinned connections to the hull were applied at the fairleads.

The first order potential solution and the second order sum-frequency QTF were computed using the Wadam software (Det Norske Veritas, 2010c). The sum-frequency force QTF has been shown to increase the tendon loads by approximately 10% in severe environmental conditions (Bachynski and Moan, 2013). It should be noted that the second order QTF solution depends on the first order motions, which were computed in Wadam from the potential flow solution with added Morison damping. As exemplified in Fig. 4, the second order long-wave FNV formulation agrees reasonably well with second order diffraction for a stationary structure (radius $a = 9$ m) up to $ka = 0.1$ (Krokstad et al., 1998), but significantly overpredicts the force in the long-wave region for the moving structure. These effects further justify using the second order QTF rather than the second-order long-wave formulation for TLPWTs.

The third order ringing force was pre-computed for the wave time history and applied as an external load at the center of the main TLPWT column at the still water line. The wave kinematics were applied as though the body were at its initial location (consistent with the implementation of the first order potential). The horizontal force was applied in the global coordinate system at the instantaneous body location.

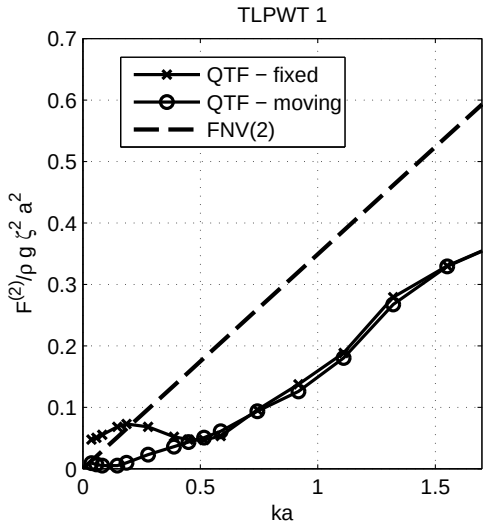

Figure 4: Double-frequency forces according to second-order diffraction (QTF) and second order FNV for TLPWT 1.

A Morison-type formulation for the viscous drag on the center column and spokes was applied to all models. The transverse drag force per length (f_D) on a vertical cylindrical section with diameter D is given by Eq. 11, where C_D is the drag coefficient, u is the transverse wave particle velocity, and v is the local transverse body velocity. Wave particle velocities were evaluated based on the first order wave input, consistent with the potential flow implementations.

$$f_D = \frac{1}{2}\rho C_D D\,(u - v)\,|u - v| \tag{11}$$

Identical transverse viscous damping coefficients were used in all models: $C_D = 0.7$ (see Eq. 11) for both circular cross sections with diameter D and square cross sections (using the width as the representative length). Although this assumption may underpredict the drag on the square cross sections, it is taken as a reasonable first approximation based on Reynolds and Keulegan-Carpenter number (Faltinsen, 1990). The effects of varying the viscous drag coefficient are discussed in Section 4.4.

The aerodynamic loads were calculated using GDW with the Beddoes-Leishman dynamic stall model for the operational turbine, while a simple lookup table was applied for the idling turbine with feathered blades. Aerodynamic drag on the tower was included in all simulations, with a transverse drag coefficient $C_D = 1.0$.

3.1. Environmental conditions

Ringing responses are associated with large wave heights (Faltinsen et al., 1995). In order to investigate conditions that are likely to induce ringing and might realistically occur in the offshore environment, a range of conditions which fall along the 3-D (H_s,T_p,U_w) 50-year contour surface of Northern North Sea conditions were chosen (Johannessen et al., 2001). Slices of the 50-year contour surface (H_s,T_p) at different wind speeds are plotted in Fig. 5.

Note that the wind speed in Fig. 5 is given for 90m, which is the assumed hub height for the NREL 5 MW wind turbine (Jonkman et al., 2009). The 90m wind speed was computed from the 10m values presented by Johannessen et al. (2001) based on a power law vertical wind speed profile with exponent 0.14 (IEC 61400-3). As shown in Fig. 5, both H_s and T_p tend to increase

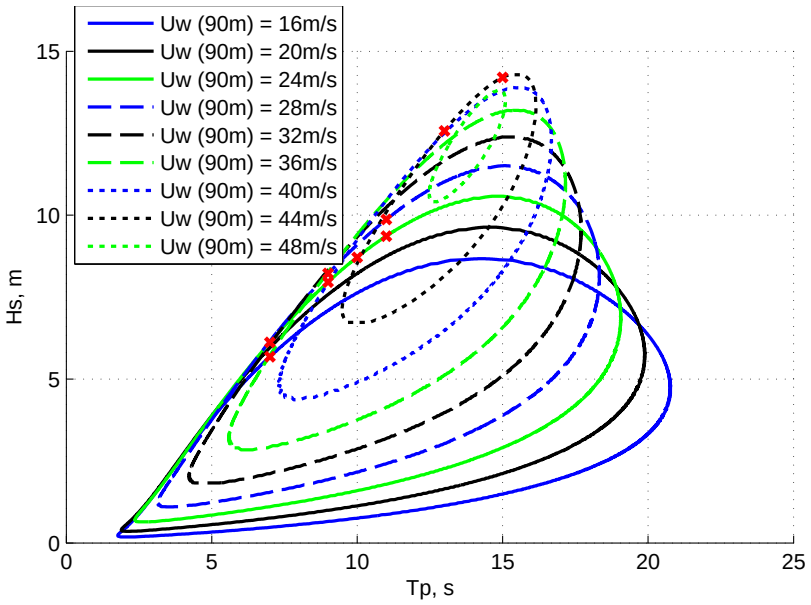

Figure 5: 50-year contours of H_s and T_p for different wind speeds, based on Johannessen et al. (2001). Markers indicate values in Table 1.

with increasing wind speed. With respect to ringing, the upper left side of the contours is the most interesting region: large wave heights and relatively short wave periods.

Based on the 50-year contours, representative environmental conditions were selected for both operational (16 and 24 m/s wind) and idling (fully feathered blades) turbine conditions (28 and 44 m/s wind), as shown in Tables 1 and 2.

Table 1: H_s given T_p and U_w, 50 year contours for the Northern North Sea

T_p (s) \ U_w (m/s)	16	24	28	44
7.0	5.68	6.12		
9.0		7.96	8.22	
10.0		8.71		
11.0	8.05	9.36	9.87	
13.0				12.57
15.0				14.20

The irregular waves were generated from a JONSWAP spectrum with the desired significant wave height, H_s, and peak period, T_p, using a frequency discretization of 0.002 rad/s. In order to avoid unphysical high-frequency first order wave excitation, the spectrum was set to zero above the wave cutoff frequency ω_c (Det Norske Veritas, 2010a):

$$\omega_c = \sqrt{2g/H_s}. \tag{12}$$

The cutoff region ($\omega_c \pm 0.25$ rad/s) was smoothed using a LOWESS method with span 0.1 rad/s. The same wave data, including the cutoff, was used for generating all orders of hydrodynamic forces.

Table 2: Conditions for each TLPWT

TLPWT 1	$D = 18$ m	10.0 s $\leq T_p \leq$ 15.0 s	$0.16 \leq ka \leq 0.36$
TLPWT 2	$D = 14$ m	9.0 s $\leq T_p \leq$ 15.0 s	$0.12 \leq ka \leq 0.35$
TLPWT 3	$D = 14$ m	9.0 s $\leq T_p \leq$ 15.0 s	$0.12 \leq ka \leq 0.35$
TLPWT 4	$D = 6.5$ m	7.0 s $\leq T_p \leq$ 11.0 s	$0.11 \leq ka \leq 0.27$

The three-dimensional wind fields were generated in NREL's TurbSim (Jonkman, 2009) based on the Kaimal spectrum with the IEC Class B normal turbulence model (NTM) (IEC 61400-1). The wind shear was modeled by the power law with exponent 0.14 (IEC 61400-3). In the vertical plane 32x32 points were used, with wind field generation time step 0.05 seconds. For each environmental condition, 10 one-hour simulations were carried out.

3.2. TLPWT models

Four baseline TLPWT models were chosen for this study, providing a range of displacements, water line diameters, and pretension values (Bachynski and Moan, 2012, 2013). The water depth was 150 m for all platforms. An overview of the baseline designs is given in Table 3 and Fig. 6.

Despite large differences in the geometry, the first natural period for combined platform pitch and tower bending was quite similar for all of the designs (≈ 2.8 s), largely due to the restrictions placed in the parametric design process (Bachynski and Moan, 2012). In order to get a better idea of the effects of ringing forces on platforms with slightly longer natural periods, a "soft" version of each design was created by decreasing the material stiffness of the tendons by an arbitrary factor. The natural periods of the original and soft concepts are given in Table 4.

Table 3: TLPWT designs

	TLPWT 1	TLPWT 2	TLPWT 3	TLPWT 4
Diameter (m)	18.0	14.0	14.0	6.5/10.0
Draft (m)	45.0	35.0	22.0	29.0
Pontoon radius (m)	27.0	32.0	28.0	25.0
Pontoon height/width (m)	2.4/2.4	5.0/5.0	6.0/6.0	6.0/6.0
Tendon diameter (m)	1.4	1.1	1.3	1.2
Tendon thickness (mm)	46.2	36.3	42.9	39.6
Displacement (m^3)	11 866	7 263	5 655	4 114
Steel mass (tonnes)	2 322	1518	1293	859
Concrete ballast (tonnes)	6456	3314	1389	506
Tendon pretension per line (F_t, kN)	6 868	4 963	8 262	5 556

In order to see the effects of the ringing forces more clearly, three hydrodynamic models were applied to each TLPWT: a first order model (P1+V), a second order model (P1+P2+V), and a model including ringing forces (P1+P2+FNV3+V). In these abbreviations, V indicates the viscous drag forces. The effects included in each model are summarized in Table 5; additional details regarding the first two models can be found in Bachynski and Moan (2013).

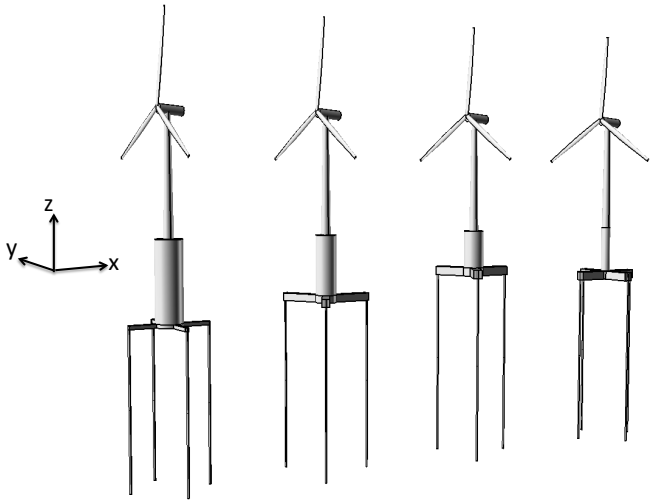

Figure 6: TLPWT designs 1-4

Table 4: Damped natural periods, including tower flexibility, based on decay tests of the FE model with parked rotor.

	TLPWT 1		TLPWT 2		TLPWT 3		TLPWT 4	
	orig.	soft	orig.	soft	orig.	soft	orig.	soft
Surge (s)	55.78	55.80	53.13	53.16	42.00	42.00	34.22	34.24
Heave (s)	0.55	1.26	0.75	2.24	0.60	2.21	0.53	1.94
Pitch/ Bend (1) (s)	2.79	3.15	2.81	3.79	2.76	4.10	2.74	4.27
Pitch/ Bend (2) (s)	0.51	1.03	0.48	1.07	0.39	0.96	0.39	0.87
Yaw (s)	13.99	14.05	18.06	18.07	18.63	18.65	19.71	19.83

3.3. Control system modification

Floating wind turbines may encounter negative feedback in above-rated wind speeds when the controller responds to the turbine motions (Skaare et al., 2007; Larsen and Hanson, 2007). TLPWTs generally have high natural frequencies in pitch, small motions at lower frequencies, and sufficient hydrodynamic damping, such that the control constants for a land-based turbine do not lead to any instability. (A surge instability is theoretically possible, but unlikely to be seen due to the the hydrodynamic damping.) When the wave-induced pitch or surge motions become large, however, there may be large variations in the rotational speed due to negative feedback. Since wave conditions associated with ringing also cause relatively large wave-frequency motions, the natural frequency of the blade pitch PI controller was reduced by modifying the controller constants, and a constant generator torque strategy above rated speed was employed in these simulations (Table 6). While this modification leads to larger variations in the generated power, it decreases the rotational speed excursions and increases the aerodynamic damping.

Furthermore, for mean wind speeds of 16 and 24 m/s, the wind turbine was assumed to remain in an operational condition regardless of gusts above the cut-out wind speed (25 m/s).

3.4. Fatigue damage estimation

Although ringing is expected to primarily affect the extreme values, simplified calculations of the fatigue damage at the tower base, tower top, and tendon fairleads were carried out in order

Table 5: Hydrodynamic models

	P1+V	P1+P2+V	P1+P2+FNV3+V
First order potential excitation	x	x	x
Added mass from the first order solution	x	x	x
Radiation damping from the first order solution	x	x	x
Second order potential sum-frequency excitation		x	x
Second order potential difference-frequency excitation			
Third order long-wave ringing forces Johannessen (2012)			x
Viscous drag (Morison formulation)	x	x	x

Table 6: Control system constants parameters (as in Jonkman et al. (2009); Jonkman (2010))

	Original (land-based)	Modified
K_I at min. pitch	0.008068634	0.00358605
K_P at min. pitch	0.01882681 s	0.0125512 s
$\omega_{\psi n}$	0.6 rad/s	0.4 rad/s
above-rated strategy	constant power	constant torque

to examine the effect of the second order wave forces and the third order ringing force on fatigue estimates. Only the axial stress (σ_x) was considered, computed as in Eq. 13, where N_x is the axial force, and M_y and M_z are the bending moments. The cross sectional area A and the area moments of inertia (I_y and I_z) were computed based on the properties of the tubular members. Values of the distances y and z corresponding to 8 points along the cross-section outer radius were considered.

$$\sigma_x = \frac{N_x}{A} + \frac{M_y}{I_y} z + \frac{M_z}{I_z} y \tag{13}$$

Stress cycles were counted using a rainflow counting technique (Matsuishi and Endo, 1968; Brodtkorb et al., 2000). Assuming a simple SN curve with slope m, the damage from N cycles was found by Palmgren-Miner's rule (Eq. 14), where K is a material property. In Eq. 14, a simple SN curve is assumed, but it is a trivial modification to select the appropriate m and K for each stress range.

$$D_{RFC} = \sum_{i=1}^{N} K^{-1} n_i S_i^m \tag{14}$$

In the present study, m and K were chosen according to bilinear SN-curves from DNV-RP-C203 (Det Norske Veritas, 2010b). For the tower, curve D from Table 2-1 (in air) was used; for the tendons, curve F from Table 2-2 (seawater with cathodic protection) was applied.

For the given collinear wind and wave conditions (wind and waves travel in the positive x-direction, as in Fig. 6), the maximum tower fatigue damage occurred at points along an axis aligned with the wind and wave direction. There was little variation in the fatigue damage at different points on the tendon cross sections, since the axial force was the dominating contributor to the stress variations. Fatigue damage results are presented as 1-hour expected values for the point with the largest damage.

4. Results

Simulation results for the baseline designs and soft designs are presented first, followed by discussions of the effects of turbine operation and variations in the viscous damping coefficient.

4.1. Baseline TLPWT designs

Figure 7 shows the 1-hour maximum tension in the downwind tendon (T_1) divided by the pretension (F_t) and the 1-hour maximum fore-aft tower base bending moment (M_{FA}) for the baseline designs. These loads, which are related to the pitch and heave motions, were most affected by ringing forces.

It should be noted that both minimum tension in the downwind line and maximum tension in the upwind line are important design qualities. In this paper, for simplicity, results for the downwind line were compared because that line is in the same position for all designs (3- and 4- legged). Presenting the minimum tension was found to be more confusing, as slack conditions occurred. Since the ringing response is oscillatory and there is little decay in the first oscillation, the maximum tension in the downwind line gives a good representation of the severity of the response.

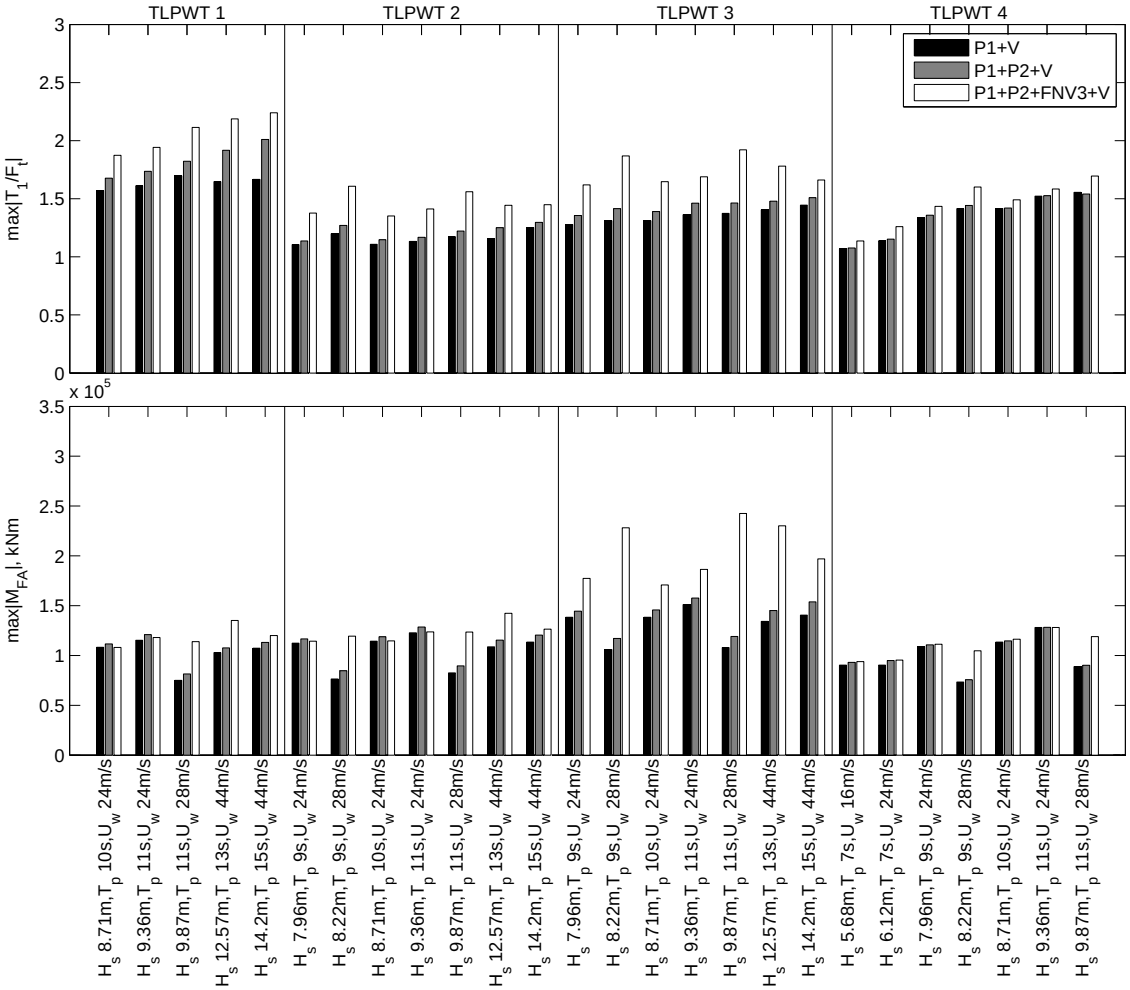

Figure 7: Baseline designs: 1-hour expected maximum tension in the downwind tendon (divided by pretension, top) and fore-aft tower base bending moment (bottom)

For TLPWT 1, the ringing forces led to negative tension incidents in all environmental conditions. The resulting tendon loads were quite large, while the tower base loads were less affected. The second order potential also caused increases in the standard deviation of tendon tension compared to the first order model, although negative tension incidents were very rare in the absence of ringing loads.

TLPWTs 2 and 3, which have the same hull waterline diameter, experienced very similar ringing loads. Ringing led to increased maximum T_1 in all of the considered environmental conditions. The maximum M_{FA} increased for TLPWT 2 in idling conditions, but was almost unchanged in operational conditions compared to the first order loads. On the other hand, the maximum M_{FA} for TLPWT 3 increased in all conditions, particularly in the idling conditions. The reason for the difference in the tower base load response between TLPWTs 2 and 3 is related to the phasing of the responses.

Fig. 8 illustrates one instance of the response to a ringing load for TLPWTs 2 and 3 in an operating condition, where there is a mean positive bending moment at the tower base due to the thrust force. The ringing force decreases M_{FA} at the peak of the first order response, but adds a peak shortly afterward. This peak is larger for TLPWT 3, which is lighter, has larger pretension, and has a smaller tendon radius. The first order variation in tension relative to pretension is smaller for TLPWT 2, but the ringing-induced variation is larger, which allows the platform to take up more of the ringing force in the tendons than in the tower base.

Ringing had a somewhat smaller impact on the maximum loads for TLPWT 4. An increase in the maximum T_1 (5-10%) was seen in all of the studied environmental conditions, and the maximum M_{FA} increased in idling conditions. The maximum M_{FA} in idling conditions was, however, still smaller than the maximum load in operational conditions.

For all of the baseline TLPWTs, ringing loads also caused an increase in the maximum tower top fore-aft bending moment in idling cases, but that moment was much smaller than the moment encountered in operating conditions. The side-side bending moments at the tower top and base, blade root bending moments, and surge and yaw motions were not strongly affected by ringing loads.

In addition to the extreme values, it is interesting to examine the effect of the ringing loads on fatigue. Fig. 9 shows the 1-hour expected fatigue damage in the downwind tendon for the baseline designs. Clearly, the load oscillations after a ringing event also contribute to fatigue. The tendon fatigue damage due to ringing is particularly large for idling cases. The fatigue damage at the tower base (not shown) follows the maximum M_{FA} patterns quite closely, with TLPWT 3 suffering the greatest increase in damage due to ringing loads. The present calculations indicate that the fatigue damage estimates for these environmental conditions are sensitive to the ringing loads, but do not consider the likelihood of encountering such environmental conditions.

Ringing also affected the fatigue at the tower top in idling conditions, but the fatigue damage there was still much smaller than during the operational cases.

4.2. Soft TLPWT designs

Figure 10 shows the 1-hour maximum of T_1 and M_{FA} for the designs with softened tendons. In general, the soft designs performed slightly worse than the stiff designs with regards to maximum loads, although TLPWT 4 did not experience very large increases in the loads. Second order forces also had a larger influence on the soft versions of TLPWTs 1-3 than on their stiff counterparts.

Comparing Figs. 7 and 10, one can see that the maximum value of M_{FA} greatly increased for soft TLPWTs 1 and 2 when ringing forces were included in the analysis. The maximum value of

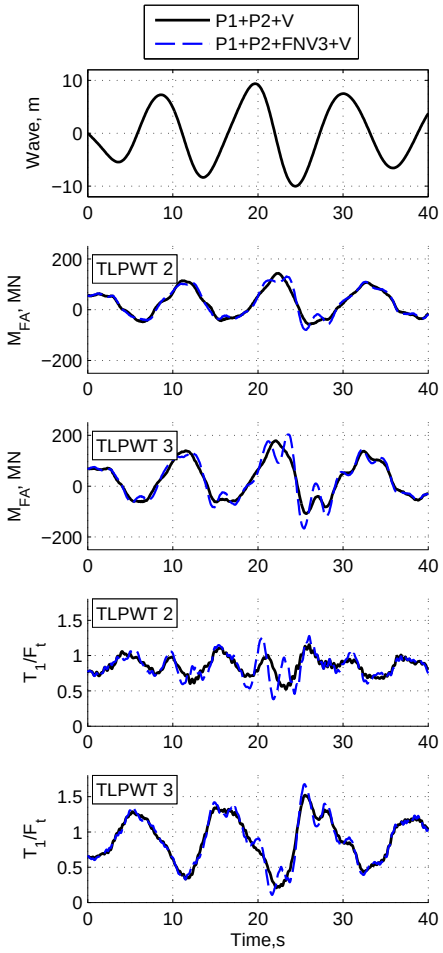

Figure 8: TLPWTs 2 and 3: first order wave elevation, fore-aft tower base bending moment, and tension in the downwind tendon (divided by pretension).

T_1 increased for the idling cases. These TLPWTs have natural pitch bending periods of 3.15 s and 3.79 s, making them particularly sensitive to the third order loads.

For the soft version of TLPWT 3, second order forces had a large effect on both T_1 and M_{FA}, but the ringing forces resulted only in a small modification to the second order results. In many conditions, the maximum response was slightly decreased by including ringing forces due to the phase difference in the forcing. The natural pitch/bending period of soft TLPWT 3 was somewhat longer than that of soft TLPWTs 1 and 2, which may place it slightly further from the third order forcing.

Similarly, Fig. 11, which shows the 1-hour expected fatigue damage in the downwind tendon for the soft designs, indicates that ringing is a particularly important consideration for soft TLPWTs 1 and 2, and that the idling cases are most critical. The tendon damage to TLPWT 3 was very dependent on the second order sum-frequency excitation, but was not very sensitive to ringing. The fatigue damage to the downwind tendon of TLPWT 4 did not depend strongly on second order or third order forces.

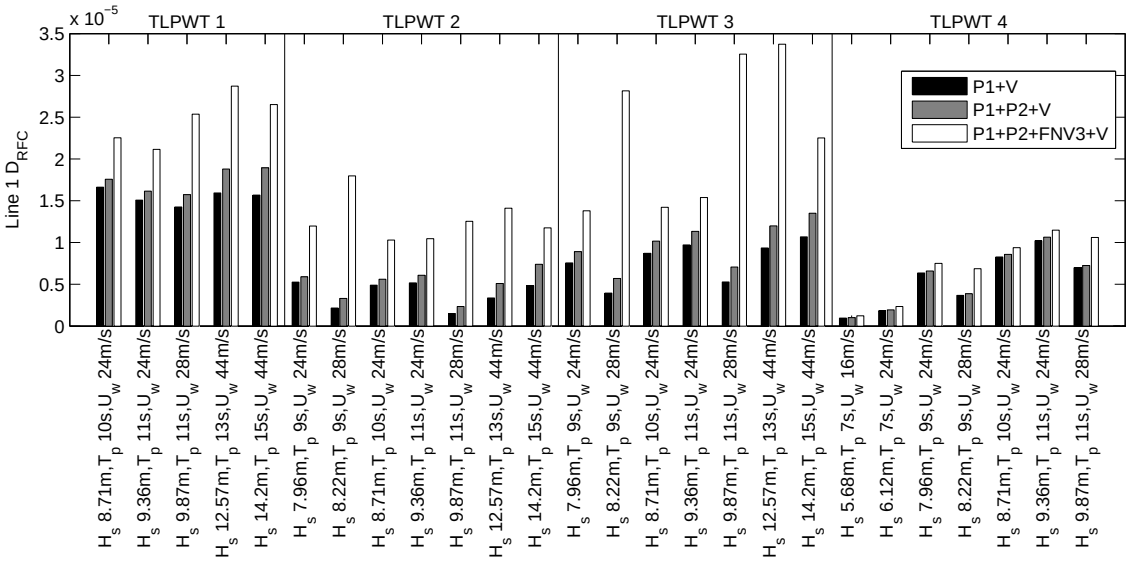

Figure 9: Baseline designs: 1-hour expected fatigue damage at the fairlead of the downwind tendon.

4.3. Operational vs. parked turbines

The previously presented results suggested that the tendon tension variation may be quite sensitive to turbine operation. The effect of turbine operation on the response to ringing loads was examined for $H_s = 8.71$ m, $T_p = 10$ s, $U_w = 24$ m/s by directly comparing simulations with identical environmental inputs and varying the turbine state. The effect of ringing loads on the expected maxima and on the 1-hour fatigue damage was computed as:

$$\Delta(x) = \frac{x(\text{P1+P2+FNV3+V}) - x(\text{P1+P2+V})}{x(\text{P1+P2+V})} \tag{15}$$

where x is the variable of interest. Fig. 12 shows the effects of ringing forces on extreme T_1 and M_{FA} and on the fatigue damage in the downwind line and tower base for the operational and idling turbine.

Ringing forces caused an increase in the maximum T_1 regardless of whether or not the turbine was operating. The increase was slightly larger for the idling turbine and for the stiff turbine designs. The effect of ringing on the tendon fatigue damage was, however, more strongly dependent on the turbine operational mode. The simulated 1-hour fatigue damage to the downwind tendon more than doubled for TLPWTs 2 and 3 in the idling condition for the assumed environmental condition, suggesting that aerodynamic damping may have an important effect on the ringing-induced short-term fatigue damage in the tendons.

The maximum M_{FA} generally increased more due to ringing when the turbine was idling than when it was operating, but the absolute maximum value was generally larger for an operating turbine (due to the contribution from the thrust force). Ringing caused a very large increase in the tower base damage for the idling turbine, further highlighting the importance of aerodynamic damping in the decay of ringing-induced oscillations.

4.4. Viscous damping effects

In order to examine the effects of viscous damping on the ringing response, simulations for a selected environmental condition were carried out for $C_D = 0.4$, 0.7, 1.0, and 1.3. The drag coefficient influences both the wave forcing and damping, but the results were not found to be

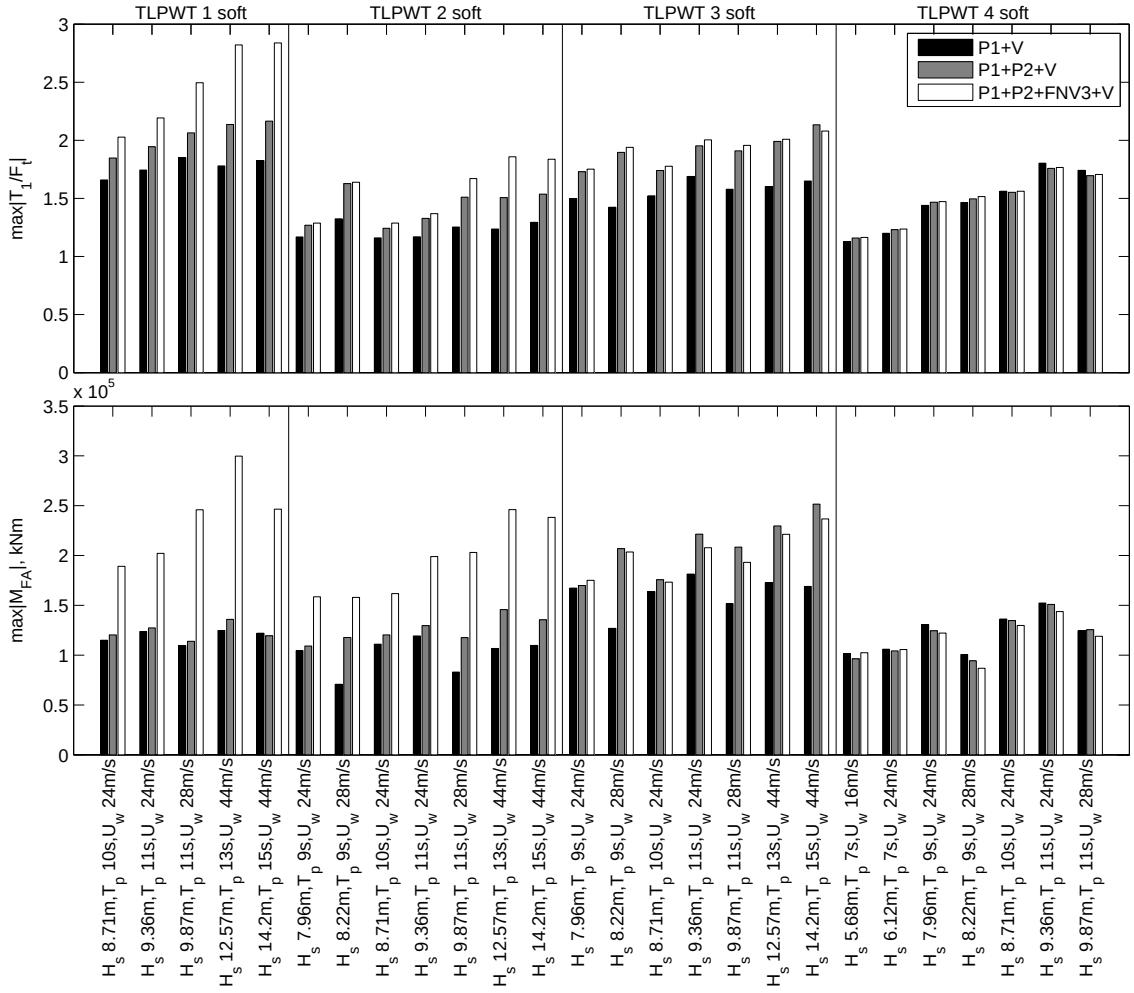

Figure 10: Soft designs: 1-hour expected maximum tension in the downwind tendon (divided by pretension, top) and fore-aft tower base bending moment (bottom)

sensitive to the value of C_D within the given range. As shown in Fig. 13, the differences in the maximum T_1 and M_{FA} were less than 3%. The effect on the fatigue damage (not shown) was similarly small.

5. Conclusions

Third order wave forces on TLPWTs can induce ringing-type responses in a range of environmental conditions which fall along the 50-year probability contour surface. The present work examines the effects of including second order and ringing forces on eight TLPWT models in both operational and idling conditions.

The implementation of the ringing forces is an important consideration. It has been shown that good agreement with experimental results requires the use of the second order QTF and the third order long-wave FNV formulation (Krokstad et al., 1998). A direct implementation of the irregular wave formulation of the FNV equation, however, includes difference-frequency terms which are not desired in the simulation and are over-conservative. By considering a single degree-of-freedom system, the effect of these low-frequency terms on the response was estimated to be

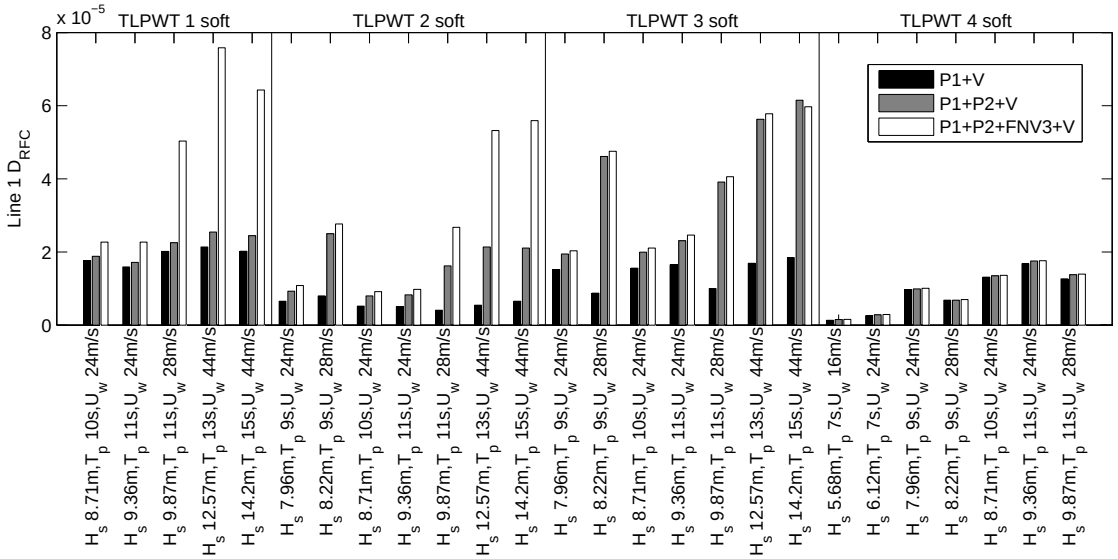

Figure 11: Soft designs: 1-hour expected fatigue damage at the fairlead of the downwind tendon.

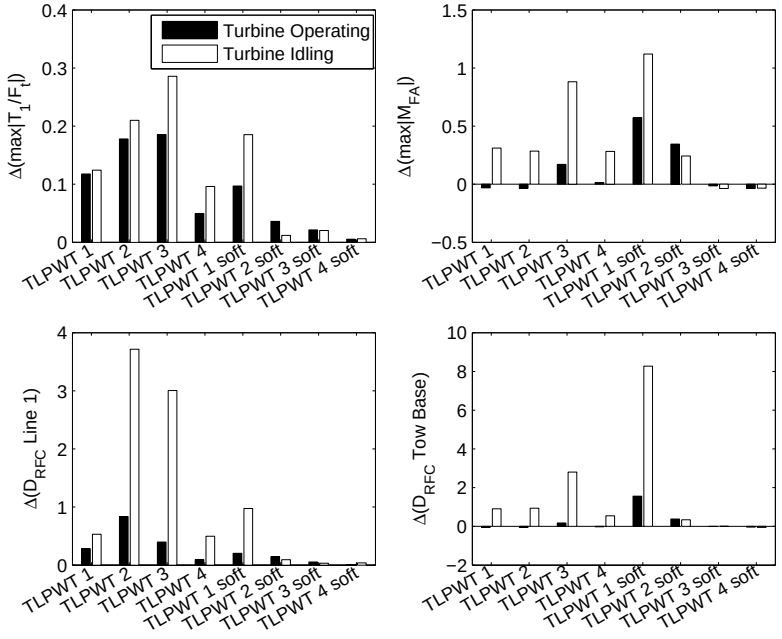

Figure 12: Effect of ringing forces on maximum T_1/F_t and M_{FA}, and on the fatigue damage in the downwind line and tower base. Relative differences are computed as in Eq. 15 for $H_s = 8.71$ m, $T_p = 10$ s, $U_w = 24$ m/s.

5-15%. In order to give the best possible estimate of the effect of ringing forces, Johannessen's implementation of the ringing force was applied here (Johannessen, 2012).

The effect of ringing forces was seen primarily in the platform pitch motions, which led to increased loads at the base of the tower and in the tendons. Ringing had little effect on surge, roll (due to the wave direction), and yaw motions, on the tower top loads, and on the blade loads.

All of the baseline (stiff) designs, with diameter 6.5-18 m and pitch/bending natural period ≈ 2.8 s, showed increased variation in the tendon tension and tower base bending moment when

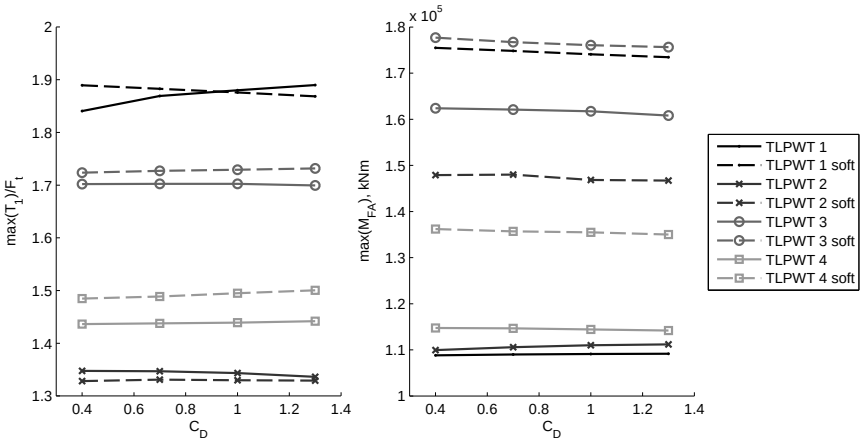

Figure 13: The 1-hour expected maximum T_1 and M_{FA} as a function of the viscous damping coefficient, C_D. Results are shown for $H_s = 8.71$ m, $T_p = 10$ s, $U_w = 24$ m/s, with the turbine operational, second order forces included, and ringing forces included.

ringing forces were included. Compared to simulations that included only the first and second order potential flow excitation, the increase in the maximum tendon tension was 12-30 % for TLPWTs 1-3 and 5-10 % for TLPWT 4 (which had the smallest diameter), and did not depend strongly on the turbine operational condition. The increase in the tower base bending moment due to ringing was largest for idling conditions ($\approx$ 30-40 % increase) and TLPWT 3 was most affected. Ringing also caused increased short-term fatigue damage to the downwind tendon and tower base, particularly in idling conditions.

The softer TLPWTs showed generally worse performance characteristics with regards to tendon tension variation and the bending moment at the tower base. Ringing forces were found to be most important for the soft versions of TLPWT 1 and 2, which had natural periods of 3.15 and 3.79 s, respectively. Second order forces were of greater importance for TLPWT 3, which had a natural period at 4.10 s. Both the extreme loads and the fatigue damage increased for the soft versions of the designs compared to the stiff versions.

Viscous damping had very little effect on the extreme loads or on the fatigue, but the aerodynamic damping caused ringing loads to have less relative effect on fatigue in the tendons and tower base for an operating turbine compared to an idling turbine.

The present study considered a limited number of environmental conditions – all of which had aligned wind and long-crested waves. The effects of structural damping on the ringing response were not examined. Although existing load models for the third order excitation may still be conservative, the present results suggest that ringing may pose a serious problem for TLPWTs in certain environmental conditions. Negative tension was encountered due to ringing loads in at least one simulation of each TLPWT studied here. TLPWT 1 showed a significant number of negative tension incidents, with somewhat more frequent occurrence for the soft version than the stiff version. Reducing the waterline diameter, increasing pretension, and further decreasing the natural periods are all methods that are expected to mitigate ringing and loss of tension. Further improvements to ringing models, additional experimental validation, and better structural models of loss-of-tension incidents should be pursued in the development of this type of platform.

Acknowledgment

Support for this work was provided by Statoil through an MIT-NTNU Gemini cooperative research project. The authors are grateful to MARINTEK for support in the development of the coupled computer code and to Dr. Jørgen Krokstad of Statkraft for valuable discussions.

References

Bachynski, E. E., Moan, T., 2012. Design considerations for tension leg platform wind turbines. Marine Structures 29, 89–114.

Bachynski, E. E., Moan, T., 2013. Hydrodynamic modeling of tension leg platform wind turbines. In: 32nd International Conference on Ocean, Offshore and Arctic Engineering. No. OMAE2013-10120.

Brodtkorb, P., Johannesson, P., Lindgren, G., Rychlik, I., Rydén, J., Sjö, E., 2000. WAFO - a MATLAB toolbox for the analysis of random waves and loads. In: Proc. 10th Int. Offshore and Polar Eng. Conf., ISOPE, Seattle, USA. Vol. 3. International Society of Offshore and Polar Engineers, pp. 343–350.

Det Norske Veritas, October 2010a. Environmental conditions and environmental loads. Tech. Rep. DNV-RP-C205.

Det Norske Veritas, 2010b. Fatigue design of offshore steel structures. Tech. Rep. DNV-RP-C203.

Det Norske Veritas, January 2010c. Wadam User Manual. 8th Edition.

Faltinsen, O., 1990. Sea Loads on Ships and Offshore Structures. Cambridge University Press.

Faltinsen, O. M., Newman, J. N., Vinje, T., 1995. Nonlinear wave loads on a slender vertical cylinder. Journal of Fluid Mechanics 289, 179–198.

Grue, J., Bjørshol, G., Strand, Ø., 1993. Higher harmonic wave exciting forces on a vertical cylinder. Tech. rep., Preprint Series, Matematisk Institutt Oslo.

Grue, J., Huseby, M., 2002. Higher-harmonic wave forces and ringing of vertical cylinders. Applied Ocean Research 24, 203–214.

Gurley, K. R., Kareem, A., May 1998. Simulation of ringing in offshore systems under viscous loads. Journal of Engineering Mechanics 124, 582–586.

Henderson, A. R., Argyriadis, K., Nichos, J., Langston, D., 2010. Offshore wind turbines on TLPs - assessment of floating support structures for offshore wind farms in German waters. In: 10th German Wind Energy Conference, Bremen, Germany.

International Electrotechnical Commission (IEC), 2005. Wind turbines: Part 1: Design requirements. Tech. Rep. IEC61400-1:2005(E).

International Electrotechnical Commission (IEC), 2009. Wind turbines: Part 3: Design requirements for offshore wind turbines. Tech. Rep. IEC61400-3.

Johannessen, K., Meling, T. S., Haver, S., 2001. Joint distribution for wind and waves in the northern North Sea. In: The 11th International Offshore and Polar Engineering Conference & Exhibition.

Johannessen, T. B., 2012. Nonlinear superposition methods applied to continuous ocean wave spectra. Journal of Offshore Mechanics and Arctic Engineering 134, 011302–1–011302–14.

Jonkman, B., September 2009. TurbSim user's guide: Version 1.50. Tech. Rep. NREL/TP-500-46198, National Renewable Energy Laboratory.

Jonkman, J., 2010. Definition of the floating system for Phase IV of OC3. Tech. Rep. NREL/TLP-500-47535.

Jonkman, J., Butterfield, S., Musial, W., Scott, G., February 2009. Definition of a 5-MW reference wind turbine for offshore system development. Tech. Rep. NREL/TP-500-38060, National Renewable Energy Laboratory.

Krokstad, J., Stansberg, C., Nestegård, A., Marthinsen, T., 1998. A new nonslender ringing load approach verified against experiments. Transactions of the ASME Journal of Offshore Mechanics and Arctic Engineering 120 (1), 20–29.

Larsen, T. J., Hanson, T. D., 2007. A method to avoid negative damped low frequent tower vibrations for a floating, pitch controlled wind turbine. Journal of Physics: Conference Series, The Second Conference on The Science of Making Torque from Wind 75.

Luxcey, N., Ormberg, H., Passano, E., 2011. Global analysis of a floating wind turbine using an aero-hydro-elastic numerical model. Part 2: Benchmark study. In: 30th International Conference on Ocean, Offshore, and Arctic Engineering. No. OMAE2011-50088.

MARINTEK, 2011a. RIFLEX User's Manual.

MARINTEK, 2011b. SIMO User's Manual.

Marthinsen, T., Stansberg, C. T., Krokstad, J. R., 1996. On the ringing excitation of circular cylinders. In: the Sixth International Offshore and Polar Engineering Conference. Vol. 1. pp. 196–204.

Matha, D., April 2009. Model development and loads analysis of an offshore wind turbine on a tension leg platform, with a comparison to other floating turbine concepts. Master's thesis, University of Colorado-Boulder.

Matsuishi, M., Endo, T., 1968. Fatigue of metals subjected to varying stress. In: Proceedings of the Kyushu Branch of Japan Society of Mechanics Engineering. pp. 37–40.

Moriarty, P. J., Hansen, A. C., 2005. AeroDyn theory manual. Tech. Rep. NREL/TP-500-36881.

Natvig, B. J., 1994. A proposed ringing analysis model for higher order tether response. In: Proceedings of the Fourth International Offshore and Polar Engineering Conference. Vol. 1. pp. 40–51.

Newman, J. N., 1996a. The second-order wave force on a vertical cylinder. Journal of Fluid Mechanics 320, 417–443.

Newman, J. N., 1996b. Waves and nonlinear processes in hydrodynamics. Kluwer, Ch. Nonlinear scattering of long waves by a vertical cylinder, pp. 91–102.

Ormberg, H., Bachynski, E. E., June 2012. Global analysis of floating wind turbines: Code development, model sensitivity and benchmark study. In: 22nd International Ocean and Polar Engineering Conference. Vol. 1. pp. 366–373.

Ormberg, H., Passano, E., Luxcey, N., 2011. Global analysis of a floating wind turbine using an aero-hydro-elastic model. Part 1: Code development and case study. In: 30th International Conference on Ocean, Offshore, and Arctic Engineering. No. OMAE2011-50114.

Rogers, N., 1998. Structural dynamics of offshore wind turbines subject to extreme wave loading. In: British Wind Energy Association 20th Annual Conference.

Schløer, S., Bredmose, H., Bingham, H., Larsen, T., 2013. Fully nonlinear wave forcing on an offshore wind turbine. structural response and fatigue. In: 10th Deep Sea Offshore Wind R&D Conference.

Skaare, B., Hanson, T. D., Nielsen, F. G., Yttervik, R., Hansen, A. M., Thomsen, K., Larsen, T. J., 2007. Integrated dynamic analysis of floating offshore wind turbines. In: 2007 European Wind Energy Conference and Exhibition.

Stansberg, C. T., 1997. Comparing ringing loads from experiments with cylinders of different diameters - an empirical study. In: 8th International Conference on the Behaviour of Off-Shore Structures (BOSS'97).

Stewart, G., Lackner, M., Robertson, A., Jonkman, J., Goupee, A., 2012. Calibration and validation of a FAST floating wind turbine model of the DeepCwind scaled tension-leg platform. In: 22nd International Offshore and Polar Engineering Conference. No. NREL/CP-5000-54822.

Tromans, P., Swan, C., Masterton, S., 2006. Nonlinear potential flow forcing: the ringing of concrete gravity based structures. Tech. Rep. Research Report 468, Health and Safety Executive.

Veldkamp, H. F., van der Tempel, J., 2005. Influence of wave modelling on the prediction of fatigue for offshore wind turbines. Wind Energy 8, 49–65.

Zang, J., Taylor, P. H., Morgan, G., Stringer, R., Orszaghova, J., Grice, J., Tello, M., 2010. Steep wave and breaking wave impact on offshore wind turbine foundations - riging re-visited. In: International Workshop on Water Waves and Floating Bodies (IWWWFB25).